Multi-step Fast Charging based State of Health Estimation of Lithium-ion Batteries

Zhang, Dayu; Wang, Zhenpo; Liu, Peng; Qin, Zian; Wang, Qiushi; She, Chengqi; Bauer, Pavol

DOI
10.1109/TTE.2023.3322582

Publication date
2024

Document Version
Final published version

Published in
IEEE Transactions on Transportation Electrification

Multistep Fast Charging-Based State of Health Estimation of Lithium-Ion Batteries

Dayu Zhang, Zhenpo Wang, *Senior Member, IEEE*, Peng Liu, *Member, IEEE*, Qiushi Wang, Chengqi She, Pavol Bauer, *Senior Member, IEEE*, and Zian Qin, *Senior Member, IEEE*

***Abstract*— Accurately predicting the battery's aging trajectory is required to ensure the safe and reliable operation of electric vehicles (EVs) and is also the fundamental technique toward residual value assessment. As a critical enabler for mainstreaming EVs, fast charging has presented formidable challenges to health prognosis technology. This study systematically compares the performance of features extracted from the multistep charging process in the state of health (SOH) assessment. First, 12 direct features are extracted from the voltage curve, and the degradation mechanisms strongly correlated to these features are analyzed in detail. Integrating the degradation mechanism and correlation analysis, a data feature construction strategy is designed to categorize extracted features into groups. Then, the performance of different features extracted from the fast charging process in the SOH assessment is compared regarding estimation accuracy. Finally, the generalization and feasibility of the optimal data feature are verified with different fast charging protocols and training data sizes. The verification results indicate that the data feature representing fused degradation modes has excellent generalization and feasibility in SOH estimation, and the mean absolute error (MAE) and root-mean-squared error (RMSE) for various cells under different decline patterns are within 0.90% and 1.10%, respectively.**

***Index Terms*— Battery, comparative study, degradation mode, multistep fast charging, state of health (SOH).**

I. Introduction

THE lithium-ion battery (LiB) has been widely used in various domains, such as energy storage, power supply, and electric vehicles (EVs), due to its high energy and power density, low self-discharge, and long lifespan. Despite the rapid drop in the cost of LiB over the last few years [1], [2], the sales of EVs still only account for 9.0% of annual passenger vehicles scales [3]. Range anxiety has been cited as one of the key reasons that restrict consumers' purchase intention. Moreover, this anxiety is compounded by the fact that the energy replenishment efficiency of EVs is significantly lower than internal combustion engine vehicles (ICEVs) [4]. Hence, the fast charging technique is regarded as the key enabler of mainstream adoption of EVs and great efforts have been devoted to developing the number and power of fast charging stations. With continuous infrastructure improvement, the EVs' fast charging frequency gradually increases, and the average monthly fast charging frequency of the public transportation field in China has exceeded 75% [5], [6].

However, numerous studies have indicated that the high charge rates of the fast charging process are likely to trigger lithium plating [7], [8], further accelerate the aging process of batteries, and even result in safety hazards. Apart from this, the complex degradation mechanisms of LiBs, intense uncertainties in practical operation, and the limitations of present measurement techniques also pose momentous challenges for accurate health assessment. Thus, developing effective feature extraction methods and diagnosing battery health from limited measurable data will offer promising improvements in preventing overcharging, ensuring safety, and supporting second-life use.

State of health (SOH) is generally used to assess the aging level of batteries from the capacity and impedance quantitatively [9]. However, measuring the capacity and impedance directly is challenging and time-consuming, especially during vehicle operation. Hence, great efforts have been devoted to exploring and improving the health state estimation techniques. Generally, the health state estimation approaches can be divided into two categories: model-based method and data-driven method [10], [11]. The model-based method relies on physics-based modeling of the degradation behavior or empirical model to describe the declining trajectory of the system [12]. For the physics-based modeling method, the electrochemical model [13], [14] and the equivalent circuit model (ECM) [15] are two commonly used battery models. The electrochemical model comprises serials of complicated, mutually coupled partial differential equations [16], which can reflect the changing process of the potential and the voltage and also describe the reaction processes inside the battery. Nevertheless, the high modeling complexity and computing

Manuscript received 1 June 2023; revised 13 August 2023; accepted 29 September 2023. Date of publication 6 October 2023; date of current version 19 September 2024. This work was supported in part by the National Natural Science Foundation of China under Grant 52072040 and in part by the China Scholarship Council under Grant 202206030133. *(Corresponding author: Zian Qin.)*

Dayu Zhang is with the National Engineering Research Center of Electric Vehicles, Beijing Institute of Technology, Beijing 100081, China, and also with the Department of Electrical Sustainable Energy, Delft University of Technology, 2628 CD Delft, The Netherlands (e-mail: dayu_zhang@bit.edu.cn).

Zhenpo Wang, Peng Liu, and Qiushi Wang are with the National Engineering Research Center for Electric Vehicles, Beijing Institute of Technology, Beijing 100811, China (e-mail: wangzhenpo@bit.edu.cn; bitliupeng@bit.edu.cn; wangqiushi@bit.edu.cn).

Chengqi She is with the Hunan Provincial Key Laboratory of Health Maintenance for Mechanical Equipment, Hunan University of Science and Technology, Xiangtan 411201, China (e-mail: shechengqi@hnust.edu.cn).

Pavol Bauer and Zian Qin are with the Department of Electrical Sustainable Energy, Delft University of Technology, 2628 CD Delft, The Netherlands (e-mail: p.bauer@tudelft.nl; zqi@ieee.org).

This article has supplementary downloadable material available at https://doi.org/10.1109/TTE.2023.3322582, provided by the authors.

Digital Object Identifier 10.1109/TTE.2023.3322582

intensiveness hinder its feasibility in practical application, and thus, some researchers have focused on improving its computational efficiency and adaptability for online applications [17], [18]. In comparison, the ECM is composed of the circuit elements that produce the same electrical behavior as the battery, which is more concise than the electrochemical model. However, the ECM lacks physical meaning and ignores the internal microcosm reactions, which is not able to depict the detailed information during the battery aging process. Moreover, the adaptive filters are generally combined with the ECMs for parameter updating [19], [20]. Distinct from the physics-based model, the empirical model ignores the internal mechanism of the batteries and is established by analyzing the mapping between the health states [e.g., capacity or internal resistance (IR)] and battery characteristics. However, such correlations obtained from historical data are sensitive to the variation in battery aging state and working conditions [12], [21]. Hence, the empirical model is also frequently combined with the filtering algorithm to update the model parameters with the latest available data [22], [23], [24]. However, the model-based method requires a large amount of historical data, and these data have put forward strict requirements for the experimental equipment and scene, which is unachievable in real-world operations. In addition, the limited model generalization ability that the model is designed for a specific system has further restricted the application of this method.

Data-driven approaches utilize historical monitoring data to predict the degradation trend of the battery without knowing its mechanisms and propagation rules precisely [25]. In contrast to the physics-based model, the data-driven method establishes a mathematical model based on only training data, avoiding the complicated modeling process. Moreover, the data-driven model is more flexible when applied to different systems, as only the parameters need to be recalibrated. Great attention from researchers worldwide has been devoted to this field, radial basis function neural network (RBFNN) [26], Gaussian process regression (GPR) [27], [28], long short-term memory network (LSTM) [29], and gated recurrent unit (GRU) network [30] are the commonly used techniques.

Except improving the machine learning techniques, the selected data feature also significantly influences the state estimation efficiency and accuracy. To comprehensively evaluate the performance of different features in SOH estimation, Jiang et al. [31] conducted a systematic comparative study with the features extracted from the broadband electrochemical impedance spectroscopy (EIS) feature, model parameter feature, and fixed-frequency impedance feature separately. The results indicate that the fixed-frequency feature has outstanding performance in SOH estimation. However, due to the cost and space constraints, installing novel sensors, which can measure EIS data or other specific signals in EVs, is unachievable at the current stage. By comparison, the battery voltage and current as the fundamental and direct measurements are preferred to generate features for health assessment. For instance, the curve-based methods, such as incremental capacity (IC) analysis [32], [33], differential voltage (DV) analysis [34], [35], and differential thermal voltage (DTV) analysis [36], [37], obtain the features from the curve generated by voltage and temperature data and exhibit remarkable performance in SOH assessment. It should be noted that the approaches mentioned above are all conducted at constant current and constant voltage (CC–CV) charging mode and have specific charging rates and temperature requirements. These inevitable limitations have directly restricted their application in multistep fast charging conditions. To solve the above restrictions, Hu et al. [38] extracted 12 features from the charging curve and then built a novel dual GPR model to predict battery pack SOH and remaining useful life (RUL) during a specific multistep charging process. However, not all the features have strong correlations with prediction accuracy, and higher dimensions of input data imply a heavier computational load, which is challenging for existing battery management system (BMS).

In view of the above, although great efforts have been devoted to battery health prognosis, most of them are designed for the CC–CV strategy or have additional requirements for the measurement technology and operating environment. In contrast, relatively few studies have focused on the performance assessment of features under fast charging conditions, especially when only voltage data are available. Furthermore, due to the charging safety strategy in the BMS, the current of each step in the multistep fast charging process is significantly affected by the charging conditions, such as battery aging status, temperature, and real-time load status of the power grid. Hence, extracting and constructing data features suitable for various fast charging scenarios is critical for battery health assessment and further promotes the widespread adoption of fast charging technologies for EVs.

To overcome these gaps, this article systematically evaluates and analyzes the performance of features extracted from the fast charging conditions and further constructs the data feature with excellent generalization for battery health estimation. This comparative study is expected to provide a reliable reference for battery management engineers to extract the most appropriate feature in SOH assessment. The main contributions are summarized as follows.

1) Focusing on the battery health estimation demand in multistep fast charging scenarios, extracting 12 highly related direct features from the voltage curve, and systematically analyzing the principal degradation mode behind each feature.
2) Based on the degradation mechanism and correlation analysis, a data feature construction strategy is designed to categorize all extracted features into different groups. The performance of different features extracted from the fast charging process in the SOH assessment is comprehensively compared for the first time.
3) The optimal data feature constructed in this work shows high generalization with different degradation patterns and changeable charging protocols, even with limited training data.

The remainder of this article is organized as follows. The detailed descriptions of the battery experimental setup and testing schedule are illustrated in Section II, followed by the details of the cells employed in this study. The fundamental techniques of battery health estimation based on different

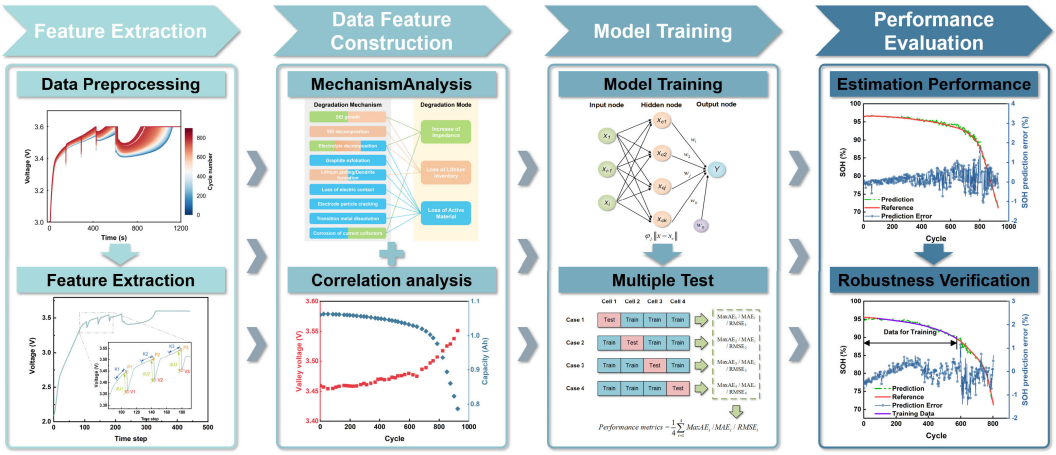

Fig. 1. Overview of the framework for this study.

TABLE I
DETAILED INFORMATION OF THE APR18650M1A LFP/GRAPHITE BATTERY

Items	Information
Nominal capacity (Ah)	1.1
Nominal voltage (V)	3.3
Ambient temperature (°C)	30
Upper cutoff voltage (V)	3.6
Lower cutoff voltage (V)	2.0
Charging protocol	Six-step, 10-minute fast charging
Discharging protocol	Constant current (4C) discharging

combinations of features are presented in Section III. Based on the works described above, the performance of each category of features in SOH assessment is analyzed and compared in Section IV, and after that, the generalization of the selected data feature is further verified. Finally, the main conclusions and subsequent research plans are summarized in Section V. An overview of the framework for this study is shown in Fig. 1.

II. CAPACITY DEGRADATION DATASET DESCRIPTION

To investigate the degradation characteristics of lithium-ion cells under fast charging protocols, the MIT-Stanford battery dataset is used in this work [39], [40]. Researchers worldwide have used this dataset to conduct extensive and in-depth studies on battery health evaluation and degradation pattern recognition for EVs [41], [42], [43]. This dataset contains the measurements of battery aging data from 169 commercial lithium-ion phosphate (LFP)/graphite cells, and the detailed information of this dataset is summarized in Table I. The standard format of six-step fast charging protocols is shown in Fig. 2(a), and the voltage and current curve during a complete fast charging process is shown in Fig. 2(b). Each protocol is defined by five constant current steps followed by one constant voltage (CV) step. The last two steps (CC5 and CV) are identical for all charging protocols. Each step comprises a 20% SOC window for the first four constant current steps, e.g., CC1 ranges from 0% to 20% SOC and CC2 ranges from 20% to 40% SOC. It is worth noting that the nominal capacity (1.1 Ah) is used throughout the test to calculate the SOC, and

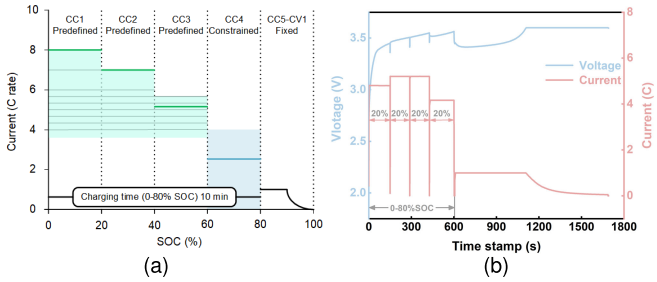

Fig. 2. Visualization of MIT-Stanford data. (a) Structure of employed six-step, 10-min fast charging protocols [39]. (b) Voltage and current curve during a complete fast charging process.

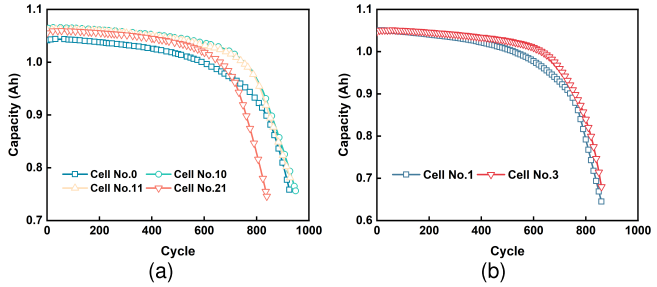

Fig. 3. Evolution trends of battery capacity under different protocols. (a) Capacity evolution trend of Cell No.0, Cell No.10, Cell No.11, and Cell No.21. (b) Capacity evolution trend of Cell No.1 and Cell No.3.

the currents used in all protocols are defined as dimensionless C rate, which means that 1C is 1.1 A or the current required to charge/discharge the nominal capacity in 1 h fully.

In this work, six cells are selected from three fast charging protocols, and the actual discharge capacity of each cycle is used to indicate their degradation state verses increased cycles. The evolution trends of battery capacity degradation under different protocols are shown in Fig. 3. In particular, Cell No.0, Cell No.10, Cell No.11, and Cell No.21 were charged with the same protocol, which will be employed in the following feature extraction, comparison, and model construction. Cell No.1 and Cell No.3 have different charging protocols, which will be utilized to verify the constructed data feature's robustness. These cells' detailed charging protocol and parameters are shown in Table II. It can be conducted from Fig. 3 that the cells with the identical fast charging protocol have better consistency in the first 600 cycles, and

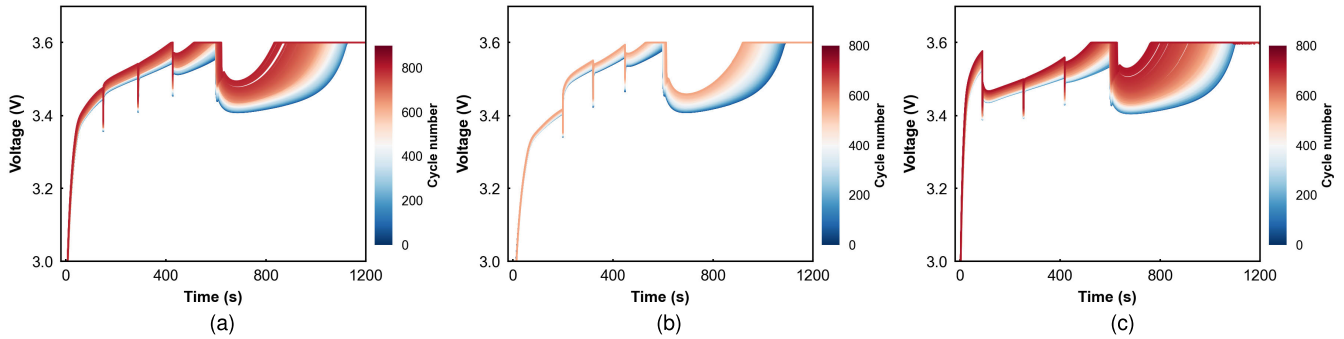

Fig. 4. Evolution trend of the charging voltage curve with increased cycles for different charging protocols. (a) Cell No.11. (b) Cell No.1. (c) Cell No.3.

TABLE II
SPECIFICATIONS OF THE SELECTED BATTERY CELLS

Cell number	Cell condition		
	Charging rate (C)	Initial voltage (V)	Initial capacity (Ah)
No.0	4.8-5.2-5.2-4.16	2.115	1.04
No.10	4.8-5.2-5.2-4.16	2.076	1.06
No.11	4.8-5.2-5.2-4.16	2.084	1.06
No.21	4.8-5.2-5.2-4.16	2.096	1.06
No.1	3.6-6.0-5.6-4.755	2.098	1.05
No.3	8.0-4.4-4.4-3.94	2.098	1.05

apparent deviations emerge between cells during the rapid decline stage of capacity. Their degradation route reveals noticeable discrepancies for cells with dissimilar fast charging protocols since the early cycling stage. The variations between the cells in the degradation process can be ascribed to the unpredictability and diversity of side reactions or/and the inconsistency of structural damage, which for the cells utilized here are primarily caused by initial manufacturing variance and different charging protocols [44]. To a certain extent, extracting and screening effective features applicable to various charging protocols is significant for SOH estimation in practical applications. It should be noted that the ratio of maximum discharge capacity to the initial capacity is defined as the SOH in this research, which is expressed as follows:

$$\mathrm{SOH}_i = \frac{C_i}{C_0} \tag{1}$$

where SOH_i means the actual SOH value at the ith cycle, C_i represents the maximum discharge capacity at the ith cycle, and C_0 is the initial capacity.

III. METHODOLOGY

In this section, we first extract features from the partial charging curve and further analyze the battery degradation mechanism characterized by these features. Based on the analysis, the extracted features are categorized into different groups according to the degradation mode and correlation

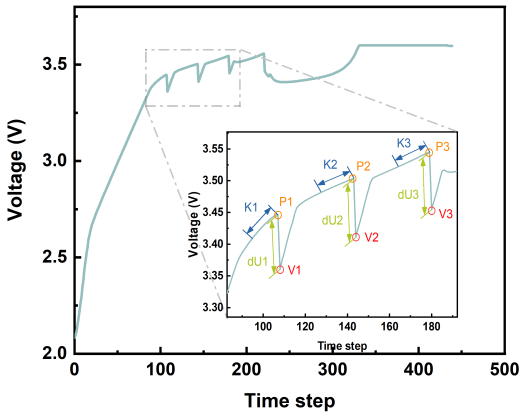

Fig. 5. Features extracted from the particle voltage curve.

analysis. After that, the RBFNN-based SOH estimation model is described in detail, and the quantitative metrics for evaluating the corresponding estimation performances are also defined.

A. Features Extraction and Description

Investigating the correlations between external characteristic signals and internal degradation mechanisms to extract useful features is highly significant for online SOH estimation. Inspired by this, 12 features strongly correlated with battery degradation are extracted from the partial fast charging curve. Fig. 4 shows the evolution trend of the charging voltage curve with increased cycles for different charging protocols. Numerous studies have categorized the degradation modes of LiBs into the loss of lithium inventory (LLI), the loss of active anode material in the electrode (LAM), and the increase of IR [10], [44]. These degradation mechanisms will directly lead to the decline of capacity and the fade of power, further reflected in the change of voltage curve during the charge and discharge processes. Notably, restricted by the upper cutoff voltage, features of the "CC4" step disappear in the late stage of the cycle. Hence, the first three steps are employed here for feature extraction, and data of this range are also more accessible in the actual charging process of EVs [45]. The 12 features acquired from the partial voltage curve are shown in Fig. 5, which will be introduced in detail next.

1) Peak Voltage of the First Three Steps ($P1$–$P3$): In the multistep fast charging process, when the SOC reaches the specified value (20%, 40%, and 60%), the voltage reaches the peak value of this stage. The essence of the LiB charging

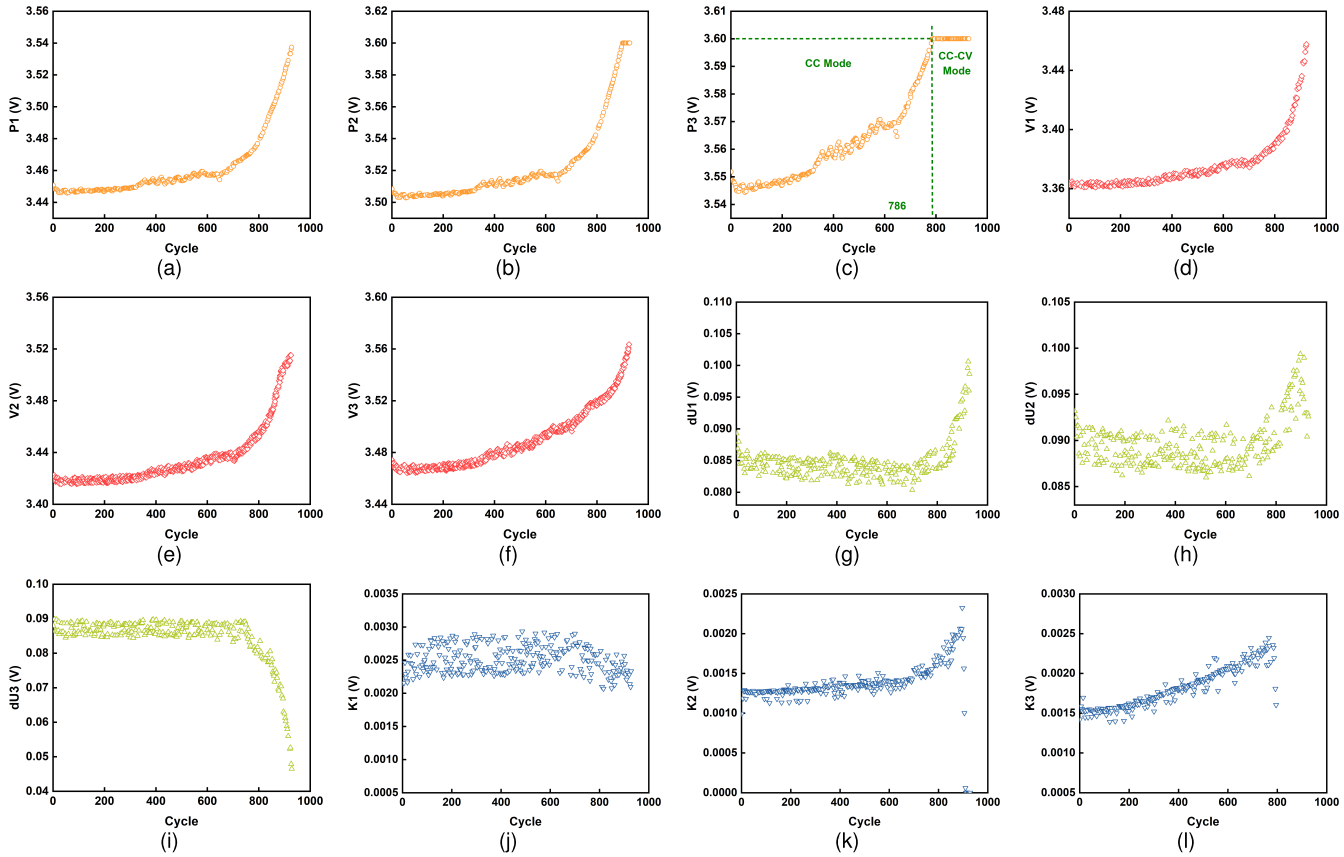

Fig. 6. Features extracted from partial voltage curve of multistep fast charging process over the whole life cycle. (a)–(c) Peak voltage. (d)–(f) Valley voltage. (g)–(i) Voltage drop. (j)–(l) Slope of charging curve.

process is the migration of Li^+ from the cathode to the anode. During this process, cathode potential increases with the decrease of lithium content, while the anode potential descends with the rise of lithium content [46]. Moreover, as the cycle increases, the formation of solid electrolyte interface (SEI) on the surface of the graphite anode, decomposition of electrolyte, and lithium plating will cause the irreversible consumption of lithium, making them unavailable for subsequent charge and discharge [10]. Thus, during the cell aging process, more Li^+ is forced to dissociate from the cathode when the same energy is injected into the cell, further enlarging the potential difference between the cathode and the anode, leading to a gradual rise of the peak voltage. Just as shown in Fig. 6(a)–(c), the peak voltages ($P1$–$P3$) of the first three steps exhibit satisfactory monotonicity over cycling. In contrast, the peak voltage of the second and third steps ($P2$ and $P3$) have remained at 3.6 V since the 900th and 787th cycles respectively, indicating that the charging mode has switched into CV mode in advance.

2) Valley Voltage of the First Three Steps ($V1$–$V3$): Whenever the SOC increases by 20%, the charging current will suddenly drop to near zero and switch to the value required by the following step [as shown in Fig. 2(b)], leading to a rapid drop in cell voltage from peak to valley. Similarly, the valley voltage reflects the potential difference between the cathode and the anode at the specified SOC. Thus, this difference will continuously enlarge with the aggravation of LLI during the cycle. It can be captured from Fig. 6(d) to (f) that the valley voltage for the first three steps increased over cycling, indicating that the energy that can be held per voltage unit is decreasing. Furthermore, the valley voltage rises more rapidly at the poststage of cycling, reflecting the trend of accelerated cell degradation at the late stage of cycling.

*3) Voltage Drop at the Current Switching Point (*dU1–dU3*):* The drop between the peak and valley voltage for each step is the response to the sudden change of charging current at the switching point. Numerous studies have proved that the IR can be measured by the voltage drop responding to a load [44], [46]. Typically, the degradation of electrodes and electrolyte materials during battery cycling will directly lead to an increase in IR. In addition, the growth and destabilization of SEI will also increase resistance. Thus, the voltage drop at the current switching point can be extracted as features and calculated as (2). As shown in Fig. 6(g)–(i), dU1 and dU2 increase relatively unremarkable at the early stage. However, both rise rapidly in the poststage. In contrast, dU3 changes not evidently in the early stage but declines more significantly in the late stage, exhibiting an opposite trend to that of dU1 and dU2. The reason for this phenomenon is that, as the cycle number increases, $P3$ rises to 3.6 V and remains constant [as shown in Fig. 6(c)], but $V3$ increases monotonously with the cycle [as shown in Fig. 6(f)] and gradually approaches the upper cutoff limit. Thus, the difference between $P3$ and $V3$ will decline to zero in the late stage

$$\mathrm{dU} = U_i - U_{i+1} \tag{2}$$

where dU is the voltage drop and U_i and U_{i+1} denote the peak voltage and valley voltage, respectively.

4) Slopes of Charging Curve of the First Three Steps ($K1$–$K3$): Due to the increase of IR during the aging process of LiBs, the voltage will rise more quickly and reach the upper cutoff sooner. Thus, the voltage increment in a fixed sampled interval will expand as the cell degrades, which can be reflected by the slope of the voltage curve in each charging step. Here, the slope is defined as (3). It can be seen from Fig. 6(j) to (l) that $K2$ and $K3$ increase monotonically with the cycle number, while $K1$ changes relatively insignificant. Moreover, it can be observed that $K2$ and $K3$ decline to zero abruptly in the late stage, which indicates that the voltage has reached the upper cutoff limit and the charging mode has switched to the CV mode

$$K = \frac{U_{i-1} - U_{i-6}}{5} \tag{3}$$

where K is the slope of the charging curve and U_{i-1} and U_{i-6} are the voltage values at points 1 and 6 before the peak voltage, respectively.

B. Correlation Analysis and Data Feature Construction

With the abovementioned feature extraction approaches, four categories of features are extracted from the partial charging curve, and each directly corresponds to certain degradation modes of the LiB. However, numerous studies have indicated that the dimension of input data will directly affect the required time consumption and calculating resources for model estimation [12], [31]. In addition, not all the features are strongly correlated with SOH, and blindly choosing the feature may diminish the estimation accuracy of SOH. Thus, conducting the correlation analysis between the extracted features and SOH is necessary for the preliminary screening of features. Considering the excellent performance of gray relational analysis (GRA) in calculating the underlying relationship even with minor and poor information [33], [47], the GRA has been employed here to quantitatively measure the relational grade between the extracted features and SOH. The basic idea of GRA is to assess the relevance between different features by describing the degree of similarity or dissimilarity of evolution trends. The steps of GRA are listed in Table III.

According to the GRA computation steps in Table III, the relational grades between the 12 extracted features and SOH for Cell No.11 are listed in Table IV as an example. Typically, the value of the relational grade being closer to 1 demonstrates that the relational degree is higher. It can be seen that the correlation coefficients for most features are higher than 0.75, except for the peak voltage at the third charging step ($P3$). Moreover, the voltage drop at the third charging step (dU3) has the highest correlation coefficients among all the features. Although all the features exhibit strong correlations to capacity degradation, extracting them all simultaneously to predict the battery SOH still proposes excellent challenges for the computational capability and efficiency of the system, especially to the BMS of real-world EVs. Given the above consideration, feature screening and combination based on correlation and degradation modes analysis are mainly conducted in this section.

TABLE III
PROCEDURES OF GRA

Step 1	**Determine the reference and comparative sequences.** For a given dataset, determine the reference sequence $Y=\{y(k)\,\vert k=1,2,3,\dots,n\}$, where $y(k)=SOH(k)$, n means the length of sequence; comparative sequence $X_i=\{x_i(k)\}$, where x_i is one of the twelve extracted features in this case, it has the same length with reference sequence.
Step 2	**Nondimensionalize the dataset.** Reduce the variation in the absolute values of the data, harmonize them to an approximate range of $(0,1)$ and focus more on their changes and trends.
Step 3	**Compute the relational coefficients $\xi_i(k)$.** The relational coefficient $\xi_i(k)$ is used to represent the closeness between $x_i(k)$ and $y(k)$, which can be deduced from $\xi_i(k)=\frac{\min_i\max_k\vert y(k)-x_i(k)\vert+\rho\max_i\max_k\vert y(k)-x_i(k)\vert}{\vert y(k)-x_i(k)\vert+\rho\max_k\max_k\vert y(k)-x_i(k)\vert}$ where ρ is the identification coefficient. $\rho\in(0,1)$, and ρ is 0.5 in this manuscript.
Step 4	**Compute the relational grade r.** The relational grade is defined as the mean value of $\xi_i(k)$: $r_i=\sum_{i=1}^{n}\xi_i(k)$

TABLE IV
GRAY RELATIONAL GRADES BETWEEN FEATURES AND SOH

Feature	Grey relational grades	Feature	Grey relational grades
$P1$	0.7702	$dU1$	0.7941
$P2$	0.7542	$dU2$	0.7543
$P3$	0.6834	$dU3$	0.9121
$V1$	0.7698	$K1$	0.7719
$V2$	0.7638	$K2$	0.8149
$V3$	0.7409	$K3$	0.8480

1) Data Feature Represents Single Degradation Mode: As deduced in Section III-A, during the aging of the LiBs, the nonreversible loss of lithium results from SEI formation, electrolyte decomposition, and lithium plating will directly cause the enlarge of potential difference between the cathode and the anode. Consequently, the peak voltage ($P1$–$P3$) and valley voltage ($V1$–$V3$) of each charging step will gradually increase with the number of cycles. Moreover, from the aspect of correlation analysis, the gray relational grades of the peak voltage and valley voltage are almost larger than 0.7 except for the peak voltage of the third step ($P3$), which is slightly lower than others. Thus, the peak voltage and valley voltage of the first three charging stages and their combination are grouped into the same category, as shown in the following equation:

$$\begin{cases} x^{\mathrm{LLI1}} = [P1,\ P2,\ P3]^T \\ x^{\mathrm{LLI2}} = [V1,\ V2,\ V3]^T \\ x^{\mathrm{LLI3}} = [P1,\ P2,\ P3,\ V1,\ V2,\ V3]^T. \end{cases} \tag{4}$$

As the widely accepted degradation mode of the LiBs, the increase of IR strongly correlates with the decline of electrodes and electrolytes, growth, and destabilization of SEI [11]. The rise in IR will directly cause the increment of the curve slope around the peak voltage ($K1$–$K3$) and the voltage drop at current switching points (dU1–dU3). In addition, the relational

grades of these features are higher than 0.75, with dU3 even exceeding 0.9, indicating the strong correlations between these features and SOH. Hence, the voltage drop and curve slope of the first three steps and their combination are employed to construct the data feature of the estimation model, which is noted in the following equation:

$$\begin{cases} x^{\mathrm{IR1}} = [\mathrm{dU1}, \mathrm{dU2}, \mathrm{dU3}]^T \\ x^{\mathrm{IR2}} = [K1, K2, K3]^T \\ x^{\mathrm{IR3}} = [\mathrm{dU1}, \mathrm{dU2}, \mathrm{dU3}, K1, K2, K3]^T. \end{cases} \tag{5}$$

2) Data Feature Represents Fused Degradation Modes: As stated previously, the degradation process of LiBs normally comprises complex physical and chemical reactions, and the main aging mechanisms at different aging stages are not exactly the same [41]. Furthermore, the relational grades for all extracted features are higher than 0.68 and are relatively close to each other. Hence, we first select all the features to construct the input vector of the estimation model, noted as x^{All} in the following equation:

$$x^{\mathrm{All}} = [P1, P2, P3, V1, V2, V3, \mathrm{dU1}, \mathrm{dU2}, \mathrm{dU3}, K1, K2, K3]^T. \tag{6}$$

As shown in Fig. 3, the capacity of all selected cells declines more evidently in the later stage of the cycle, indicating that the slight deviations of features will cause noticeable errors. From this aspect, the peak voltages of the second and third steps ($P2$ and $P3$), which remain constant in the later stage of the cycle due to the predefined charge protection protocols, will directly affect the accuracy of SOH assessment in the later phases. In contrast, the valley voltages for the first three steps ($V1$–$V3$) represent a similar degradation mode to peak voltages and have no plateau over the cycling. Furthermore, according to the correlation analysis results of GRA and Pearson correlation analysis (provided in the Supplementary Material), the third step's curve slope and voltage drop have the highest gray relational grades among the features of identical categories. Hence, the second feature extracted from hybrid degradation modes is constructed and noted as x^{Fused} in the following equation:

$$x^{\mathrm{Fused}} = [V1, V2, V3, \mathrm{dU3}, K3]^T. \tag{7}$$

It is important to specify here that the constructed data features and the degradation mechanisms do not necessarily have one-to-one correspondence, and their relationships may be many-to-many. However, it is difficult to consider them all comprehensively, and we focus more on the dominant degradation mechanisms behind the data features instead, which also facilitates a more reasonable classification of the features.

C. Description of RBFNN

This study aims to comprehensively compare the performance of different features in health estimation for fast charging application scenarios, so an effective machine learning method is necessary. An artificial neural network typically comprises an input layer, certain hidden layers, and an output layer. The number of hidden layers and their nodes can be configured in specific situations. In contrast, the RBF networks are typically built with one hidden layer with nonlinear activation functions and a linear output layer. This more straightforward structure makes them possess the best approximation property and can be trained with substantially faster procedures, further exhibiting satisfactory performance in battery SOH assessment. Here, the schematic of the RBF network is shown in Fig. 7(a).

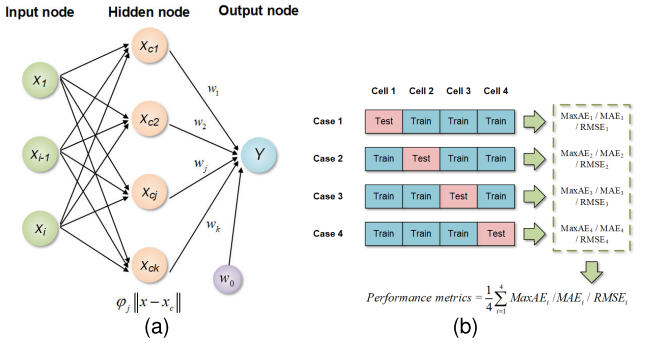

Fig. 7. Basic techniques for SOH estimation. (a) Schematic of the RBF network. (b) Diagram of the multiple test.

The input node contains the selected features x, whereas the SOH for each cycle (Y) is associated with the output node. The output node collects the nonlinear output from a generic number M of hidden nodes, and each one is weighted by the factor w_j and the bias w_0. In addition, each hidden node includes a basic function ϕ, which provides a nonlinear activation dependent on the distance between the input data and prototype vector, hereafter referred to as the basic function center (x_c). The output function of the RBF network in Fig. 7(a) is calculated as

$$Y = \sum_{j=1}^{M} w_j \varphi_j \|x - x_c\| + w_0. \tag{8}$$

In this article, the Gaussian function shown as (9) is utilized, and (8) can thus be written as

$$\varphi_j \|x - x_c\| = \exp\left(\frac{-\|x - x_c\|^2}{2\sigma_j^2}\right) \tag{9}$$

$$Y = \sum_{j=1}^{M} w_j \exp\left(\frac{-\|x - x_c\|^2}{2\sigma_j^2}\right) + w_0 \tag{10}$$

where σ is the standard deviation of the Gaussian function, which denotes the width of the RBF kernel.

During the training process, the center value x_c, the bias w_0, and the weights w_j, which connect the hidden layer to the output layer, need to be iteratively optimized. In this research, the gradient descent method is employed to solve the fitting problem, and the learning rate is set as 0.01 on the trial-and-error method. The root-mean-squared-based loss function is noted as

$$\mathrm{Loss} = \frac{1}{2}\sum_{i=1}^{s} (y^i - y_p^i)^2 \tag{11}$$

where y^i and y_p^i represent the actual SOH of training samples and the model estimation, respectively, and S denotes the number of samples contained in the training dataset. As the iterations increased, these parameters are updated as follows:

$$\begin{cases} w_j(i) = w_j(i-1) + \eta(y^i - y_p^i) + \alpha(w_j(i-1) \\ \qquad -w_j(i-2)) \\ \sigma_j(i) = \sigma_j(i-1) + \eta\Delta\sigma_j + \alpha(\sigma_j(i-1) - \sigma_j(i-2)) \\ x_{cj}(i) = x_{cj}(i-1) + \eta\Delta x_{cj} + \alpha(x_{cj}(i-1) - x_{cj}(i-2)) \end{cases} \tag{12}$$

where w_j, σ_j, and x_{cj} denote the weight, standard deviation, and center value of the jth hidden node, respectively, i represents the number of iterations, and η and α are the learning rate and momentum factor that both take values among [0, 1], respectively.

In addition, the number of hidden neurons (M) is generally determined by the complexity of the relationship that needs to be learned. In light of the generalization and efficiency of neural network, the number of hidden neurons has been empirically set to 100 on a trial-and-error procedure.

D. Performance Metrics

To comprehensively compare the performance of different combinations of features in SOH estimation, the maximum absolute error (MaxAE), mean absolute error (MAE), and root-mean-squared error (RMSE) are employed in this study, which is defined as follows:

$$\begin{cases} \text{MaxAE} = \max(|y_i - \widehat{y}_i|) \\ \text{MAE} = \dfrac{1}{N}\displaystyle\sum_{i=1}^{N} |y_i - \widehat{y}_i| \\ \text{RMSE} = \sqrt{\dfrac{1}{N}\displaystyle\sum_{i=1}^{N} (y_i - \widehat{y}_i)^2} \end{cases} \tag{13}$$

where y_i and $\widehat{y}_i$ are the reference and estimated values, respectively.

The multiple test is employed to comprehensively evaluate the performance of different data features, as shown in Fig. 7(b). Especially for each category of features, the estimation process will repeat four times. Each time, a different cell will be considered the target domain, the remaining cells will be regarded as the source domain, and the output of the RBF network is cell SOH.

IV. Comparative Analysis of SOH Estimation

In this section, the performance of the constructed data features in battery SOH estimation will first be quantitatively compared. Then, the robustness of the selected data feature is further verified under changeable charging protocols.

A. Estimation Example 1: SOH Estimation Based on x^{LLI} and x^{IR}

As mentioned in Section III-B, x^{LLI} and x^{IR} have strong correlations with the LLI and the increase of IR during the degradation of the battery, respectively. The performance of SOH estimation based on these two categories of features is shown in Tables V and VI. Based on the multiple test, each estimation study contains four training and test cases, and then, the estimation results of four cells are obtained.

TABLE V
Performance Indicators for Each Study Based on x^{LLI}

Data feature	Cell No.	Performance indicators		
		MaxAE (%)	MAE (%)	RMSE (%)
x^{LLI1}	No.0	5.09	2.31	2.28
	No.10	6.28	0.54	1.01
	No.11	3.45	0.53	0.69
	No.21	2.85	0.96	0.98
	Average	**4.42**	**1.09**	**1.24**
x^{LLI2}	No.0	4.18	1.66	1.67
	No.10	5.92	0.99	1.38
	No.11	2.08	0.33	0.45
	No.21	2.27	0.60	0.81
	Average	**3.61**	**0.90**	**1.08**
x^{LLI3}	No.0	4.25	1.99	2.23
	No.10	7.04	0.71	1.24
	No.11	1.94	0.34	0.50
	No.21	1.92	0.33	0.43
	Average	**3.79**	**0.84**	**1.09**

TABLE VI
Performance Indicators for Each Study Based on x^{IR}

Data feature	Cell No.	Performance indicators		
		MaxAE (%)	MAE (%)	RMSE (%)
x^{IR1}	No.0	14.82	4.84	5.21
	No.10	17.06	2.90	4.07
	No.11	8.39	1.58	2.02
	No.21	7.91	1.75	2.11
	Average	**12.04**	**2.77**	**3.35**
x^{IR2}	No.0	14.15	1.22	1.52
	No.10	11.03	0.88	1.22
	No.11	10.91	0.78	1.21
	No.21	7.45	1.04	1.44
	Average	**10.89**	**0.98**	**1.35**
x^{IR3}	No.0	3.66	1.79	1.89
	No.10	8.87	1.06	1.56
	No.11	4.81	0.49	0.60
	No.21	5.21	0.67	1.02
	Average	**5.64**	**1.01**	**1.27**

First, according to the degradation mechanisms analysis, three kinds of data features related to LLI are constructed, and the detailed results are shown in Table V. Regarding average performance metrics, the estimation results for all three data features are close to each other, with the average MaxAE lower than 5.00%, which can basically satisfy the practical requirements. Moreover, among these three studies, the estimation using x^{LLI2} exhibits the best performance in the dimensions of MaxAE and RMSE, followed by the estimation using x^{LLI3} and the estimation based on x^{LLI1} performs the worst. This implies that the introduction of peak voltage plays a slightly negative role in health status assessment. From the

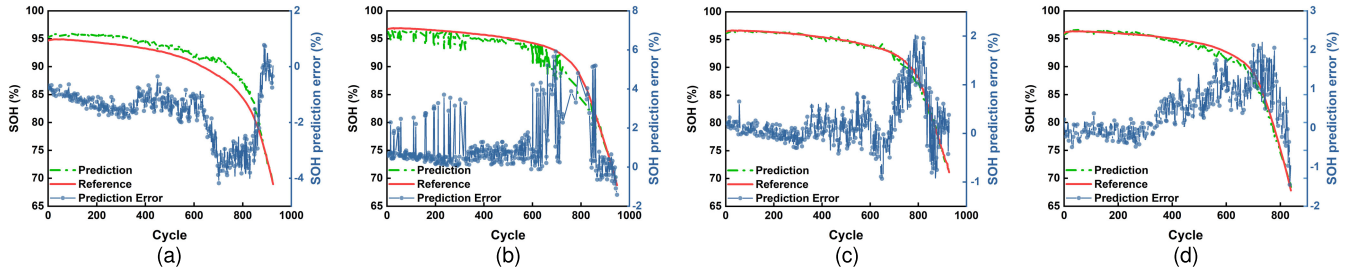

Fig. 8. Battery SOH estimation results based on x^{LLI2}. (a)–(d) Estimation results of Cell No.0, Cell No.10, Cell No.11, and Cell No.21, respectively.

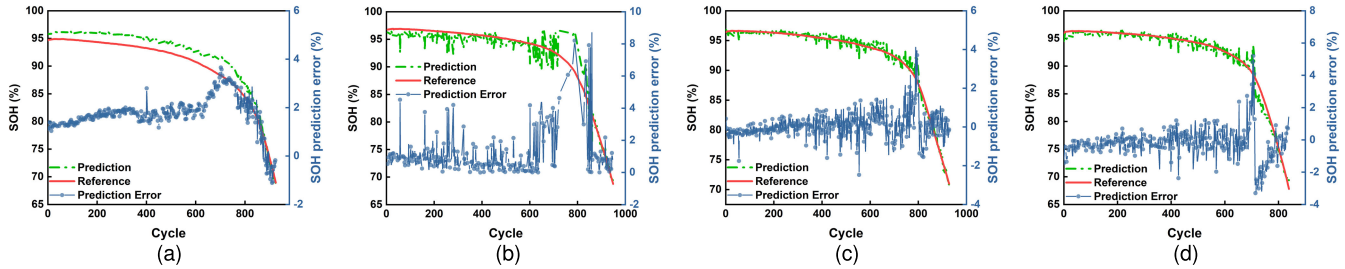

Fig. 9. Battery SOH estimation results based on x^{IR3}. (a)–(d) Estimation results of Cell No.0, Cell No.10, Cell No.11, and Cell No.21, respectively.

estimation of each cell concretely, the performance metrics of Cell No.11 and Cell No.21 in all three studies are significantly better than other cells in the same study. Taking the estimations based on x^{LLI2} as an example, the estimated values of Cell No.11 and Cell No.21 have accurately reflected the degradation trends of cells [as shown in Fig. 8(c) and (d)], and the MaxAE of these two cases is both within 2.30%. Compared to this, the estimated values for Cell No.0 and Cell No.10 [as shown in Fig. 8(a) and (b)] deviate relatively much from reference values, with MaxAE of cell No.0 and Cell No.10 having reached 4.18% and 5.92%, respectively. From a purely mathematical perspective, the deviation in SOH estimation may arise from the different mapping relationships between the training and test data, whereas from the characteristics of the battery itself, the essence of these differences is the discrepancies in degradation patterns caused by manufacturing deviations. However, regarding global stability, the RMSE and MAE of all cases in this estimation example are less than 2.50%, indicating that the estimation results for all the cells exhibit good agreement with the reference value during the whole life cycle.

Second, as mentioned in Section III-B, three kinds of data features are constructed by features that strongly correlate with the change of IR, and the relational grades of these features are higher than others. The quantitative metrics of these three studies are presented in Table VI. Regarding the averaged estimation performance, the difference in estimation accuracy between these three data features is more prominent. The estimation using x^{IR3} achieves the best accuracy of the three in all metrics, especially in the aspect of MaxAE, which reaches 5.64%, while the studies using x^{IR1} and x^{IR2} both exceed 10.00%. This indicates that not all the features in x^{IR1} and x^{IR2} are strongly correlated to SOH, and the combination of strongly correlated features has a significant positive impact on battery health estimation. Specific to each cell estimation case, similar to the x^{LLI}-based SOH estimation studies, due to the inconsistencies of the degradation pattern caused by inevitable manufacturing bias, there exist significant differences in SOH estimation performance between cells. As shown in Fig. 9(c) and (d), the estimated SOH of Cell No.11 and Cell No.21 using x^{IR3} trace the trajectory of referenced SOH more accurately, and the optimal estimation accuracy happens in the estimation of Cell No.11, with the RMSE and MAE both lower than 1%. From the average performance indicator of each estimation study, the estimations based on x^{LLI} exhibit better accuracy than that using x^{IR}, and this phenomenon is more pronounced for Cell No.11 and Cell No.21, implying that relying exclusively on the results of correlation analysis for feature selection has certain limitations. Actually, the magnitude of correlation coefficients does not only depend on the relevance between the features and the SOH, but the employed correlation analysis method will also influence it to some extent. Taking the GRA used in this study as an example, which assesses the correlations by studying the geometric proximity between different curves [33], [47]. Thus, the features (e.g., dU1 and dU2 and $K1$ and $K2$), which have similar decline trends with SOH, are assigned higher relational grades. Moreover, as shown in Fig. 6, the convergence of features dUi and Ki is significantly weaker than Pi and Vi, resulting in dramatic fluctuations of estimated values based on x^{IR}.

B. Estimation Example 2: SOH Estimation Based on x^{All} and x^{Fused}

According to the statements in Section III-B, the constructed data features x^{All} and x^{Fused} contain the features that represent different degradation modes, and the estimation results are shown in Figs. 10 and 11.

For the x^{All}-based SOH estimation study shown in Fig. 10, which can be conducted using all the features extracted from the charging curve, it can achieve acceptable precision. During the whole life cycle of these four cells, Cell No.11 and

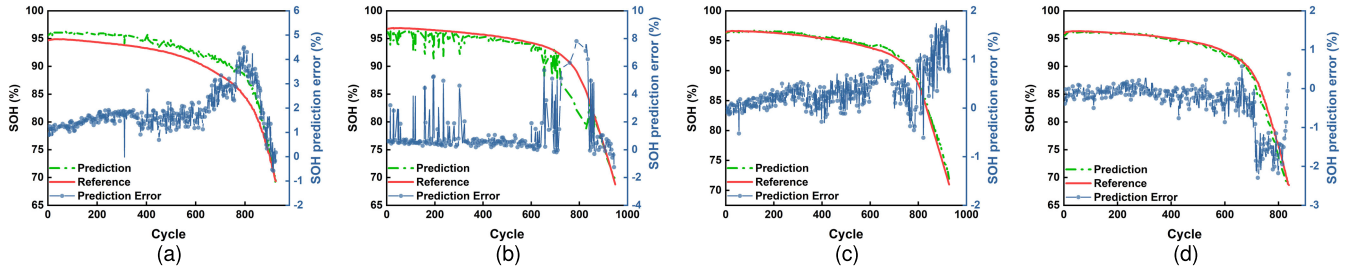

Fig. 10. Battery SOH estimation results based on x^{All}. (a)–(d) Estimation results of Cell No.0, Cell No.10, Cell No.11, and Cell No.21, respectively.

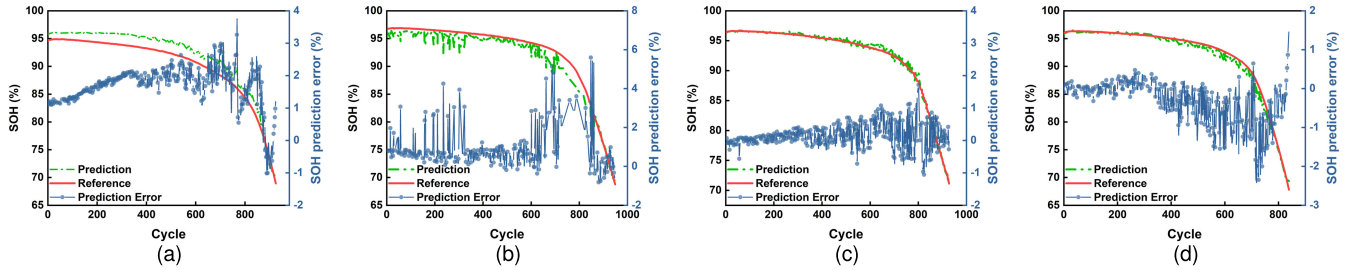

Fig. 11. Battery SOH estimation results based on x^{Fused}. (a)–(d) Estimation results of Cell No.0, Cell No.10, Cell No.11, and Cell No.21, respectively.

TABLE VII

PERFORMANCE INDICATORS FOR EACH STUDY BASED ON x^{All} AND x^{Fused}

Data feature	Cell No.	Performance indicators		
		MaxAE (%)	MAE (%)	RMSE (%)
x^{All}	No.0	4.49	1.84	2.00
	No.10	7.81	0.67	1.17
	No.11	1.86	0.38	0.53
	No.21	2.29	0.41	0.68
	Average	**4.11**	**0.91**	**1.2**
x^{Fused}	No.0	3.84	1.72	1.90
	No.10	5.59	0.91	1.21
	No.11	1.71	0.27	0.38
	No.21	2.49	0.44	0.67
	Average	**3.41**	**0.84**	**1.04**

Cell No.21 have better estimation performance with MaxAE both lower than 2.30%. At the same time, the maximum error appears in the estimation of Cell No.0, with the RMSE and MAE reaching 2.00% and 1.84%, respectively. In terms of the average estimation error, the x^{All}-based estimation result is comparable with that of x^{LLI2} in all three indicators, and both are significantly preferable to the estimation based on x^{IR}. Furthermore, as shown in Fig. 11, the estimated SOHs based on x^{Fused} for all cells track the trajectories of real SOHs further precisely. Primarily, the averaged MaxAE, RMSE, and MAE based on x^{Fused} have improved to that using features representing single degradation mode (the MaxAE is 3.41%, the RMSE is 1.04%, and the MAE is 0.84%). Although x^{Fused} is constructed with only five features, it has superior performance compared to x^{All}, which contains 12 features, and the enhancements of MaxAE and RMSE exceeded 17.00% and 13.00%, respectively. The detailed results are summarized in Table VII. From the discussion of these two estimation examples, it can be concluded that the input data constructed by features representing different degradation modes exhibit excellent performance in SOH assessment. This further indicates that the coupling of multiple degradation mechanisms generally influences the decline process of the battery. In addition, according to the comparison of the above estimation examples, it can be found that not the higher dimensions of input data, the better the estimation effect. In contrast, taking the nonstrongly correlated features into the input data might negatively impact the battery health estimation. Finally, the estimation study using x^{Fused} has achieved optimal accuracy with fewer features compared to other studies, significantly reducing computational and storage requirements for onboard applications.

It should be clarified here that when applying the features extracted from voltage-related curves to real-world operating conditions, due to the effect of temperature on the battery aging rate, these features will fluctuate locally with periodic temperature changes [48]. However, the correlations between the features and battery health status will not be significantly influenced [49]. In other words, when applying these feature extraction methods to changeable temperature conditions, we can leverage the powerful nonlinear fitting capabilities of the machine learning methods and use the temperature and features as model inputs to accomplish the battery health prognostics tasks [32].

C. Robustness Verification Under Changeable Multistep Fast Charging Protocols

Sections IV-A and IV-B has verified the feasibility of the constructed data features under a specific multistep fast charging protocol. However, during practical applications, the current of each charging step will change dynamically with the real-time load state of the power grid and the charging protection strategy of BMS. Hence, verifying the robustness of the constructed data feature in changeable fast charging conditions is remarkable for subsequent real-world applications.

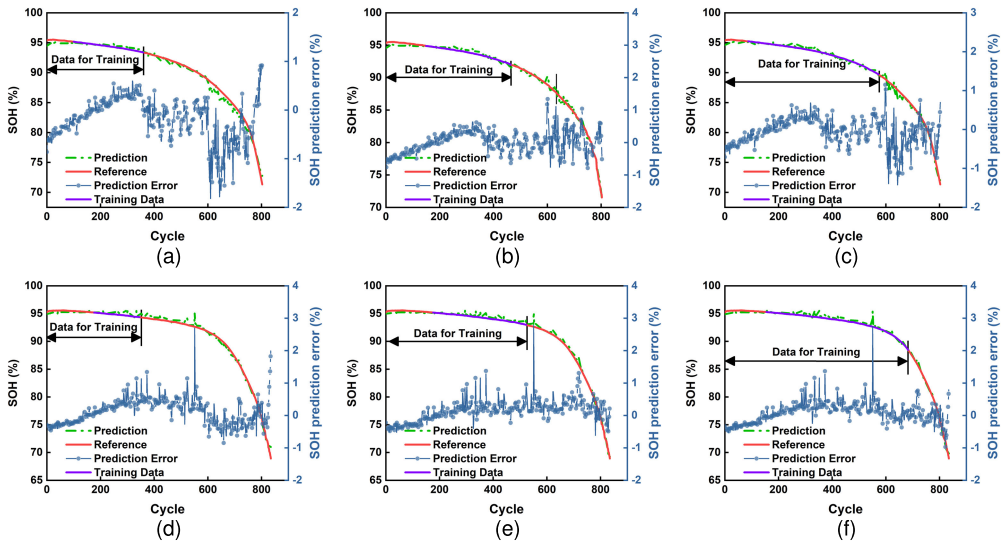

Fig. 12. Battery SOH estimation results with different fast charging protocol and training data sizes. (a)–(c) Estimation results of cell No.1 with 20%, 40%, and 60% training data, respectively. (d)–(f) Estimation results of cell No.3 with 20%, 40%, and 60% training data, respectively.

TABLE VIII
PERFORMANCE INDICATORS FOR CASES WITH DIFFERENT TRAINING DATA SIZES AND FAST CHARGING PROTOCOLS

Charging rate (C)	Training size (%)	Performance indicators		
		MaxAE (%)	MAE (%)	RMSE (%)
3.6-6.0-5.6-4.755	20	1.49	0.29	0.38
	40	1.33	0.28	0.36
	60	1.88	0.37	0.50
8.0-4.4-4.4-3.94	20	2.82	0.26	0.35
	40	2.86	0.29	0.38
	60	2.78	0.33	0.43

In this section, two estimation studies based on different fast charging protocols are carried out, and both take x^{Fused} as the data feature. In addition, the whole life cycle data of Cell No.1 and Cell No.3 are selected to reflect the characteristics of the corresponding fast charging protocol. The training data size is set to 20%, 40%, and 60%. The estimated results are shown in Fig. 12, and the MaxAE, MAE, and RMSE of predicted results are summarized in Table VIII. It can be seen from Fig. 12 that the expected value has tracked the decline path of reference value smoothly and satisfactorily. According to the performance indicators shown in Table VIII, the MaxAE, MAE, and RMSE of both studies are less than 3.00%, 0.40%, and 0.50%, respectively. Moreover, an evident situation is found that not the higher the training data size, the better the estimation accuracy. In contrast, the difference in estimation accuracy for different training data sizes is insignificant. Overall, the accuracy of both cells with the training data size not exceeding 40% is superior to that of 60% training data size. More nearly, the MAE and RMSE of Cell No.3 with 20% training data size are superior to 40% training data size. This situation indicates that the data feature and SOH estimation model developed in this research have excellent robustness and reliability when facing changeable fast charging protocols and achieve satisfactory estimation results even with a small training data size. These capabilities make it a favorable application prospect for battery health estimation of new energy vehicles.

V. CONCLUSION

This study systematically evaluates the performance of different direct features for battery SOH estimation toward multistep fast charging scenarios. Twelve features are extracted from the first three fast charging steps of the voltage curve, and these features are further categorized into four kinds of data features based on the correlation analysis and the degradation mechanisms strongly related to them. Taking RBFNN to construct the estimation model, the MaxAE, MAPE, and RMSE are leveraged to gauge the performance of each data feature. The verification results indicate that all constructed data features except x^{IR} have an excellent generalization for different cells with different degradation paths. The averaged maximum deviation among the whole life cycle is within 4.50%, which can satisfy many industrial applications that typically require the error to be around 5.00% [50]. In addition, the comparison of all estimation studies indicates that x^{Fused}, which is constructed by features representing different degradation modes, has performed optimally on all performance metrics simultaneously, with the MaxAE, MAE, and RMSE of 3.41%, 0.84%, and 1.04%, respectively. Furthermore, the constructed data feature x^{Fused} is verified under different charging protocols. The MAE and RMSE for both charging scenes are less than 0.4% and 0.5%, respectively, even with only 20% experimental data used for model training. Considering the same degradation mechanisms among the commonly used LiBs [51] and the excellent generalization of current change point-based features [38], the proposed methods are also suitable for other types of LiBs, which provides remarkable support for selecting and constructing optimal data features for battery health estimation in fast charging applications.

In further research, the effects of data sampling situations, operating environments, and driving behaviors on feature extraction and model construction will be considered in depth.

REFERENCES

[1] N. Collath, B. Tepe, S. Englberger, A. Jossen, and H. Hesse, "Aging aware operation of lithium-ion battery energy storage systems: A review," *J. Energy Storage*, vol. 55, Nov. 2022, Art. no. 105634. [Online]. Available: https://www.sciencedirect.com/science/article/pii/S2352152X2201622X

[2] X. G. Yang, G. Zhang, S. Ge, and C. Y. Wang, "Fast charging of lithium-ion batteries at all temperatures," *Proc. Nat. Acad. Sci. USA*, vol. 115, no. 28, pp. 7266–7271, Jul. 10 2018.

[3] BNEF. *Bloomberg New Energy Finance (2022) Electric Vehicle Outlook 2018*. Accessed: Nov. 25, 2022. [Online]. Available: https://about.bnef.com/electric-vehicle-outlook/#toc-download

[4] H. Tu, H. Feng, S. Srdic, and S. Lukic, "Extreme fast charging of electric vehicles: A technology overview," *IEEE Trans. Transp. Electrific.*, vol. 5, no. 4, pp. 861–878, Dec. 2019.

[5] Z. Wang, *Annual Report on the Big Data of New Energy Vehicle in China*. Beijing, China: China Machine Press, 2023.

[6] H. He et al., "China's battery electric vehicles lead the world: Achievements in technology system architecture and technological breakthroughs," *Green Energy Intell. Transp.*, vol. 1, no. 1, Jun. 2022, Art. no. 100020.

[7] X. Lin, K. Khosravinia, X. Hu, J. Li, and W. Lu, "Lithium plating mechanism, detection, and mitigation in lithium-ion batteries," *Prog. Energy Combustion Sci.*, vol. 87, Nov. 2021, Art. no. 100953.

[8] G. Zhu et al., "Fast charging lithium batteries: Recent progress and future prospects," *Small*, vol. 15, no. 15, pp. 1805389–30869836, Apr. 2019.

[9] A. Barré, B. Deguilhem, S. Grolleau, M. Gérard, F. Suard, and D. Riu, "A review on lithium-ion battery ageing mechanisms and estimations for automotive applications," *J. Power Sources*, vol. 241, pp. 680–689, Nov. 2013.

[10] Y. Li et al., "Data-driven health estimation and lifetime prediction of lithium-ion batteries: A review," *Renew. Sustain. Energy Rev.*, vol. 113, Oct. 2019, Art. no. 109254.

[11] R. Xiong, Y. Pan, W. Shen, H. Li, and F. Sun, "Lithium-ion battery aging mechanisms and diagnosis method for automotive applications: Recent advances and perspectives," *Renew. Sustain. Energy Rev.*, vol. 131, Oct. 2020, Art. no. 110048.

[12] X. Hu, L. Xu, X. Lin, and M. Pecht, "Battery lifetime prognostics," *Joule*, vol. 4, no. 2, pp. 310–346, Feb. 2020.

[13] D. F. Wang, Q. Zhang, H. Q. Huang, B. W. Yang, H. S. Dong, and J. M. Zhang, "An electrochemical-thermal model of lithium-ion battery and state of health estimation," *J. Energy Storage*, vol. 47, Mar. 2022, 103528.

[14] W. Vermeer, G. R. Chandra Mouli, and P. Bauer, "A comprehensive review on the characteristics and modeling of lithium-ion battery aging," *IEEE Trans. Transp. Electrific.*, vol. 8, no. 2, pp. 2205–2232, Jun. 2022.

[15] L. Zhang, H. Peng, Z. Ning, Z. Mu, and C. Sun, "Comparative research on RC equivalent circuit models for lithium-ion batteries of electric vehicles," *Appl. Sci.*, vol. 7, no. 10, p. 1002, Sep. 2017.

[16] M. A. Rahman, S. Anwar, and A. Izadian, "Electrochemical model parameter identification of a lithium-ion battery using particle swarm optimization method," *J. Power Sources*, vol. 307, pp. 86–97, Mar. 2016.

[17] R. Xiong, L. Li, Z. Li, Q. Yu, and H. Mu, "An electrochemical model based degradation state identification method of lithium-ion battery for all-climate electric vehicles application," *Appl. Energy*, vol. 219, pp. 264–275, Jun. 2018.

[18] J. Li, L. Wang, C. Lyu, H. Wang, and X. Liu, "New method for parameter estimation of an electrochemical-thermal coupling model for LiCoO2 battery," *J. Power Sources*, vol. 307, pp. 220–230, Mar. 2016.

[19] A. Guha and A. Patra, "Online estimation of the electrochemical impedance spectrum and remaining useful life of lithium-ion batteries," *IEEE Trans. Instrum. Meas.*, vol. 67, no. 8, pp. 1836–1849, Aug. 2018.

[20] L. Wang, J. Ma, X. Zhao, X. Li, K. Zhang, and Z. Jiao, "Adaptive robust unscented Kalman filter-based state-of-charge estimation for lithium-ion batteries with multi-parameter updating," *Electrochim. Acta*, vol. 426, Sep. 2022, Art. no. 140760.

[21] L. Lam and P. Bauer, "Practical capacity fading model for li-ion battery cells in electric vehicles," *IEEE Trans. Power Electron.*, vol. 28, no. 12, pp. 5910–5918, Dec. 2013.

[22] J. Kim, S. Lee, and B. H. Cho, "Complementary cooperation algorithm based on DEKF combined with pattern recognition for SOC/Capacity estimation and SOH prediction," *IEEE Trans. Power Electron.*, vol. 27, no. 1, pp. 436–451, Jan. 2012.

[23] C. Lyu, Q. Lai, T. Ge, H. Yu, L. Wang, and N. Ma, "A lead-acid battery's remaining useful life prediction by using electrochemical model in the particle filtering framework," *Energy*, vol. 120, pp. 975–984, Feb. 2017.

[24] C. F. Pan, Y. Chen, L. M. Wang, and Z. G. He, "Lithium-ion battery remaining useful life prediction based on exponential smoothing and particle filter," *Int. J. Electrochem. Sci.*, vol. 14, no. 10, pp. 9537–9551, 2019.

[25] K. Liu, Z. Wei, C. Zhang, Y. Shang, R. Teodorescu, and Q.-L. Han, "Towards long lifetime battery: AI-based manufacturing and management," *IEEE/CAA J. Autom. Sinica*, vol. 9, no. 7, pp. 1139–1165, Jul. 2022.

[26] C. She, Y. Li, C. Zou, T. Wik, Z. Wang, and F. Sun, "Offline and online blended machine learning for lithium-ion battery health state estimation," *IEEE Trans. Transp. Electrific.*, vol. 8, no. 2, pp. 1604–1618, Jun. 2022.

[27] K. Liu, Y. Shang, Q. Ouyang, and W. D. Widanage, "A data-driven approach with uncertainty quantification for predicting future capacities and remaining useful life of lithium-ion battery," *IEEE Trans. Ind. Electron.*, vol. 68, no. 4, pp. 3170–3180, Apr. 2021.

[28] Z. Deng, X. Hu, P. Li, X. Lin, and X. Bian, "Data-driven battery state of health estimation based on random partial charging data," *IEEE Trans. Power Electron.*, vol. 37, no. 5, pp. 5021–5031, May 2022.

[29] Z. Chen, X. Y. Song, R. X. Xiao, J. W. Shen, and X. L. Xia, "State of health estimation for lithium-ion battery based on long short term memory networks," in *Proc. Joint Int. Conf. Energy, Ecol. Environ. ICEEE, Electr. Intell. Vehicles (ICEIV)*, 2018, pp. 21–25.

[30] Y. Fan, F. Xiao, C. Li, G. Yang, and X. Tang, "A novel deep learning framework for state of health estimation of lithium-ion battery," *J. Energy Storage*, vol. 32, Dec. 2020, Art. no. 101741.

[31] B. Jiang, J. Zhu, X. Wang, X. Wei, W. Shang, and H. Dai, "A comparative study of different features extracted from electrochemical impedance spectroscopy in state of health estimation for lithium-ion batteries," *Appl. Energy*, vol. 322, Sep. 2022, Art. no. 119502.

[32] C. She, Z. Wang, F. Sun, P. Liu, and L. Zhang, "Battery aging assessment for real-world electric buses based on incremental capacity analysis and radial basis function neural network," *IEEE Trans. Ind. Informat.*, vol. 16, no. 5, pp. 3345–3354, May 2020.

[33] X. Li, Z. Wang, L. Zhang, C. Zou, and D. D. Dorrell, "State-of-health estimation for li-ion batteries by combing the incremental capacity analysis method with grey relational analysis," *J. Power Sources*, vols. 410–411, pp. 106–114, Jan. 2019.

[34] P. Mohtat, S. Lee, J. B. Siegel, and A. G. Stefanopoulou, "Comparison of expansion and voltage differential indicators for battery capacity fade," *J. Power Sources*, vol. 518, Jan. 2022, Art. no. 230714.

[35] S. Zhang, X. Guo, X. Dou, and X. Zhang, "A rapid online calculation method for state of health of lithium-ion battery based on Coulomb counting method and differential voltage analysis," *J. Power Sources*, vol. 479, Dec. 2020, Art. no. 228740.

[36] Y. Merla, B. Wu, V. Yufit, N. P. Brandon, R. F. Martinez-Botas, and G. J. Offer, "Novel application of differential thermal voltammetry as an in-depth state-of-health diagnosis method for lithium-ion batteries," *J. Power Sources*, vol. 307, pp. 308–319, Mar. 2016.

[37] Z. Wang, C. Yuan, and X. Li, "Lithium battery State-of-Health estimation via differential thermal voltammetry with Gaussian process regression," *IEEE Trans. Transp. Electrific.*, vol. 7, no. 1, pp. 16–25, Mar. 2021.

[38] X. Hu, Y. Che, X. Lin, and Z. Deng, "Health prognosis for electric vehicle battery packs: A data-driven approach," *IEEE/ASME Trans. Mechatronics*, vol. 25, no. 6, pp. 2622–2632, Dec. 2020.

[39] P. M. Attia et al., "Closed-loop optimization of fast-charging protocols for batteries with machine learning," *Nature*, vol. 578, no. 7795, pp. 397–402, Feb. 2020.

[40] K. A. Severson et al., "Data-driven prediction of battery cycle life before capacity degradation," *Nature Energy*, vol. 4, no. 5, pp. 383–391, Mar. 2019.

[41] H. You et al., "Nonlinear health evaluation for lithium-ion battery within full-lifespan," *J. Energy Chem.*, vol. 72, pp. 333–341, Sep. 2022.

[42] Z. Zhou, Y. Liu, M. You, R. Xiong, and X. Zhou, "Two-stage aging trajectory prediction of LFP lithium-ion battery based on transfer learning with the cycle life prediction," *Green Energy Intell. Transp.*, vol. 1, no. 1, Jun. 2022, Art. no. 100008. [Online]. Available: [Online]. Available: https://www.sciencedirect.com/science/article/pii/S2773153722000081

[43] Y. Zhang, T. Wik, J. Bergström, M. Pecht, and C. Zou, "A machine learning-based framework for online prediction of battery ageing trajectory and lifetime using histogram data," *J. Power Sources*, vol. 526, Apr. 2022, Art. no. 231110.

[44] C. R. Birkl, M. R. Roberts, E. McTurk, P. G. Bruce, and D. A. Howey, "Degradation diagnostics for lithium ion cells," *J. Power Sources*, vol. 341, pp. 373–386, Feb. 2017.
[45] D. Cui et al., "Battery electric vehicle usage pattern analysis driven by massive real-world data," *Energy*, vol. 250, Jul. 2022, Art. no. 123837.
[46] D. Ren et al., "An electrochemical-thermal coupled overcharge-to-thermal-runaway model for lithium ion battery," *J. Power Sources*, vol. 364, pp. 328–340, Oct. 2017.
[47] D. Yang, X. Zhang, R. Pan, Y. Wang, and Z. Chen, "A novel Gaussian process regression model for state-of-health estimation of lithium-ion battery using charging curve," *J. Power Sources*, vol. 384, pp. 387–395, Apr. 2018.
[48] L. Zhou, Y. Zhao, D. Li, and Z. Wang, "State-of-Health estimation for $LiFePO_4$ battery system on real-world electric vehicles considering aging stage," *IEEE Trans. Transp. Electrific.*, vol. 8, no. 2, pp. 1724–1733, Jun. 2022.
[49] T. Waldmann, M. Wilka, M. Kasper, M. Fleischhammer, and M. Wohlfahrt-Mehrens, "Temperature dependent ageing mechanisms in lithium-ion batteries—A post-mortem study," *J. Power Sources*, vol. 262, pp. 129–135, Sep. 2014.
[50] Y. Zhang and Y.-F. Li, "Prognostics and health management of lithium-ion battery using deep learning methods: A review," *Renew. Sustain. Energy Rev.*, vol. 161, Jun. 2022, Art. no. 112282.
[51] S. Pelletier, O. Jabali, G. Laporte, and M. Veneroni, "Battery degradation and behaviour for electric vehicles: Review and numerical analyses of several models," *Transp. Res. B, Methodol.*, vol. 103, pp. 158–187, Sep. 2017.

Dayu Zhang was born in Hebei, China, in 1993. He received the B.S. and M.S. degrees in mechanical engineering from Chang'an University, Xi'an, China, in 2017 and 2020, respectively. He is currently pursuing the Ph.D. degree in mechanical engineering with the National Engineering Laboratory for Electric Vehicles, Beijing Institute of Technology, Beijing, China.

His research interests mainly include the modeling and health state assessment of lithium-ion batteries and big data analysis.

Zhenpo Wang (Senior Member IEEE) received the B.Eng. degree in mechanical design and manufacturing from Tongji University, Shanghai, China, in 2000, and the Ph.D. degree in automotive engineering from the Beijing Institute of Technology, Beijing, China, in 2005.

He is currently a Professor with the School of Mechanical Engineering and the Director of the National Engineering Research Center for Electric Vehicles, Beijing Institute of Technology. His research interests include big data technology, battery safety management, wireless charging systems, and advanced vehicle chassis control for electric vehicles.

Prof. Wang serves as the Executive Editor-in-Chief for *Journal of Green Energy and Intelligent Transportation*. He is also on the Editorial Board of *China Journal of Highway and Transport*.

Peng Liu (Member, IEEE) received the Ph.D. degree in mechanical engineering from the Beijing Institute of Technology, Beijing, China, in 2011.

He is currently an Associate Professor with the School of Mechanical Engineering, Beijing Institute of Technology. His current research interests include battery fault diagnosis, intelligent transportation, and big data analysis.

Qiushi Wang received the B.S. degree in automotive engineering from Southwest Jiaotong University, Chengdu, China, in 2017. He is currently pursuing the Ph.D. degree in mechanical engineering with the National Engineering Laboratory for Electric Vehicles, Beijing Institute of Technology, Beijing, China.

His research interests mainly include battery health management and big data analysis of electric vehicles.

Chengqi She received the Ph.D. degree in mechanical engineering from the Beijing Institute of Technology, Beijing, China, in 2022.

He is currently an Associate Professor at the Hunan Provincial Key Laboratory of Health Maintenance for Mechanical Equipment, Hunan University of Science and Technology, Xiangtan, China. His research interests include modeling and state of health estimation of lithium-ion batteries based on real-world big data.

Pavol Bauer (Senior Member, IEEE) received the master's degree in electrical engineering from the Technical University of Košice, Košice, Slovakia, in 1985, and the Ph.D. degree in power electronics from the Delft University of Technology, Delft, The Netherlands, in 1995.

From 2002 to 2003, he was with KEMA (DNVGL), Arnhem, The Netherlands. He is currently a Full Professor with the Department of Electrical Sustainable Energy and the Head of the DC Systems, Energy Conversion, and Storage Group, Delft University of Technology. He is also a Professor with the Brno University of Technology, Brno, Czech Republic, and an Honorary Professor with the Politehnica University Timişoara, Timişoara, Romania. He has authored/coauthored eight books and more than 120 journal articles and 500 conference papers. He holds seven international patents and organized several tutorials at international conferences. He has participated in several Leonardo da Vinci and H2020, and Electric Mobility Europe EU projects as a Project Partner (ELINA, INETELE, E-Pragmatic, Micact, Trolley 2.0, OSCD, P2P, and Progressus) and a Coordinator (PEMCWebLab.com-Edipe, SustEner, and Eranet DCMICRO). He has worked on many projects for the industry concerning wind and wave energy, and power electronic applications for power systems, such as Smarttrafo; and HVdc systems, projects for smart cities such as photovoltaic (PV) charging of electric vehicles, PV and storage integration, and contactless charging.

Dr. Bauer is a member of the Executive Committee of European Power Electronics Association and the International Steering Committee at numerous conferences, the former Chairperson of the Benelux IEEE Joint Industry Applications Society and the Power Electronics and Power Engineering Society Chapter, and the Chairperson of the Power Electronics and Motion Control Council.

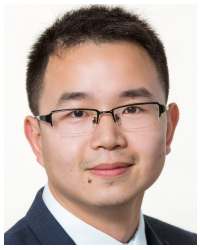

Zian Qin (Senior Member, IEEE) received the B.Eng. degree in electrical engineering from Beihang University, Beijing, China, in 2009, the M.Eng. degree in electrical engineering from the Beijing Institute of Technology, Beijing, in 2012, and the Ph.D. degree in electrical engineering from Aalborg University, Aalborg, Denmark, in 2015.

He is an Assistant Professor with the Delft University of Technology, Delft, The Netherlands. In 2014, he was a Visiting Scientist at Aachen University, Aachen, Germany. He has published more than 100 journals/conference papers, four book chapters, two international patents, and also worked on several European and Dutch national projects in these areas. His research interests include power quality and stability of power electronics-based grids, and solid-state transformers.

Dr. Qin is an Associate Editor of IEEE TRANSACTIONS INDUSTRIAL ELECTRONICS, and a Guest Associate Editor of IEEE TRANSACTIONS POWER ELECTRONICS, IEEE JOURNAL OF EMERGING AND SELECTED TOPICS and IEEE TRANSACTIONS ENERGY CONVERSION. He is a Distinguished Reviewer for 2020 of IEEE TRANSACTIONS OF INDUSTRIAL ELECTRONICS. He served as the Technical Program Chair of IEEE-PEDG 2024, IEEE-PEDG 2023, IEEE-ISIE 2020, IEEE-COMPEL 2020, etc.